Analog memristive devices based on La2NiO4+δ as synapses for spiking neural networks

Thoai-Khanh Khuu, Aleksandra Koroleva, Arnaud Degreze, Elena-Ioana Vatajelu, Gauthier Lefèvre, Carmen Jiménez, Serge Blonkowski, Eric Jalaguier, Ahmad Bsiesy, Mónica Burriel

Analog Memristive Devices based on $La_2NiO_{4+\delta}$ as Synapses for Spiking Neural Networks

Thoai-Khanh Khuu[1,2], Aleksandra Koroleva[1,3], Arnaud Degreze[1,3], Elena-Ioana Vatajelu[3], Gauthier Lefèvre[2], Carmen Jiménez[1], Serge Blonkowski[4], Eric Jalaguier[4], Ahmad Bsiesy[2] and Mónica Burriel[1,*]

[1] Université Grenoble Alpes, CNRS, Grenoble INP, LMGP, Grenoble, France
[2] Université Grenoble Alpes, CNRS, CEA/LETI Minatec, LTM, Grenoble, France
[3] Université Grenoble Alpes, CNRS, Grenoble INP, TIMA, Grenoble, France
[4] Université Grenoble Alpes, CEA, LETI, Grenoble, France

*Email: Monica.Burriel@grenoble-inp.fr

Received xxxxxx
Accepted for publication xxxxxx
Published xxxxxx

Abstract

Neuromorphic computing has recently emerged as a potential alternative to the conventional von Neumann computer paradigm, which is inherently limited due to its architectural bottleneck. Thus, new artificial components and architectures for brain-inspired computing hardware implementation are required. Bipolar analog memristive devices, whose resistance (or conductance) can be continuously tuned (as a synaptic weight), are potential candidates for artificial synapse applications. In this work, lanthanum nickelate ($La_2NiO_{4+\delta}$, L2NO4), a mixed ionic electronic conducting oxide, is used in combination with TiN and Pt electrodes. The TiN/L2NO4/Pt devices show bipolar resistive switching with gradual transitions both for the SET and RESET processes. The resistance (conductance) can be gradually modulated by the pulse amplitude and duration, showing good data retention characteristics. A linear relationship between the resistance change and total applied pulse duration is experimentally measured. Moreover, synaptic depression and potentiation characteristics, one of the important functions of bio-synapses, are artificially reproduced for these devices, then modeled and successfully tested in a spiking neural network environment. These results indicate the suitability of using TiN/L2NO4/Pt memristive devices as long-term artificial synapses in neuromorphic computing.

Keywords: resistive switching, artificial synapse, neuromorphic computing, lanthanum nickelate, La_2NiO_4, spiking neural network (SNN), valence change memory (VCM), mixed-ionic electronic conductor

1. Introduction

Artificial neural networks (ANN), brain-inspired computational architectures, have recently drawn considerable attention due to their fault tolerance and ability to learn processes or complicated tasks in artificial intelligence (AI) systems [1]. At the same time, many AI and machine learning applications are performed in software, which runs on conventional computation architecture. However, most on-market computers are based on the von Neumann architecture which is facing its drawbacks. Indeed, the limited *bandwidth* caused by the physical separation between the central processing unit (CPU) and memory unit in this architecture leads to many limits in the data processing procedure and thus makes the computational performance lower, especially when computing on large sets of data (e.g., learning tasks in ANN) [2]. On top of that, Moore's law is approaching

its end because of the physical limit of miniaturization, thus the ANN tasks running on CMOS-based computers with an enormous amount of transistors are not executed efficiently. Therefore, there is an urgent need for novel computation architectures.

Neuromorphic computing systems that emulate the bio-physics of neurons and synapses in the human brain are expected to have very high energy efficiency and might be thus potential candidates for the new generation of beyond von Neumann paradigms [3,4]. The human brain consists of a great number of neurons and synapses, which are interconnected. Therefore, to construct an efficient neuromorphic computing system, the development of artificial elements to mimic the biological functions of synapses is a prerequisite. Synaptic plasticity, the capacity to modulate the synaptic weight, is one of the crucial properties that must be mimicked. Besides, long-term synaptic dynamics (long-term potentiation and depression, i.e., LTP/LTD) are also key features in neuromorphic computing, especially for learning and memory, making the artificial synapse remember important information.

During the last decades, redox-based valence change memristive devices have become a very hot topic both in academia and in industry, presenting a very wide range of potential opportunities for different computing technologies, especially as random access memories and artificial synapses [5,6]. The prospects of these novel devices cover technological applications from non-volatile high-density memories to advanced architectures for near- or even in-memory computing [7,8], opening the way to the hardware implementation of already existing neuromorphic software solutions used for machine learning applications and deep learning, in particular [9,10]. Among all these technologies, the highest potential gain is expected to occur by moving from state-of-the-art von Neumann architecture to new disruptive computing paradigms that are biologically inspired, with envisioned applications that span from ANN to real-time signal processing, robotics and cognitive reasoning [10]. Memristive devices that show an analog tunability of states in a wide range of resistance values, together with low energy consumption of the writing/reading processes and compact nanoscale dimensions, are considered very promising candidates for building high-density neuromorphic systems [7,9].

Valence-Change Memories (VCMs) are typically composed of an oxide material sandwiched between two different electrodes. The resistive switching in these devices is induced by the drift of oxygen anions (or metal cations in some cases) upon the application of an external bias, triggering redox reactions and, therefore, a change of valence in the cation sublattice [11,12]. These reactions can occur locally in a single filament, at the whole metal/oxide interface, or, in an intermediate case, in interconnected regions or multiple filaments [13]. VCMs can be either volatile or non-volatile depending on the device and operation mode, with time constants that can be tailored by interface engineering and have proven to be able to mimic both synapse-like and neuron-like functions [10]. While the most commonly used materials for VCMs are high-k binary oxides (HfO_2 [14–18], TiO_2 [19–22] and Ta_2O_5 [23–27]), ternary oxides such as perovskites with ABO_3 structure (e.g. titanates [13,28,29], manganites [30,31], ruthenates [32] and cobaltites [33,34]), in which the oxidation state of the B cation can change to accommodate oxygen vacancies, are particularly interesting candidates for interface-type switching devices (i.e. showing area scaling). $Pr_{1-x}Ca_xMnO_3$ (PCMO)-based memristive devices have, for example, show forming-free, interface-type analog memory capabilities and are currently the most widely used perovskite-based devices for neuromorphic engineering. These devices have already been used as analog synapses for pattern recognition [35], as integrate-and-fire (IF) neurons [36] and as stochastic neurons [37].

Several studies reported on the VCM capabilities of memristive devices based on La_2NiO_4 (L2NO4), a perovskite-related structure, using an ohmic Pt electrode and an active (i.e. easily oxidizable) Ti counter electrode (forming a rectifying and tunable Schottky contact) [38,39]. L2NO4 was selected as Mixed Ionic Electronic Conducting (MIEC) oxide due to its large oxygen mobility [40,41] to facilitate the storage and exchange of oxygen with the active electrode material (Ti). A gradual highly multilevel analog-type bipolar resistive switching, desirable for neuromorphic computing, was measured in Ti/L2NO4/Pt planar heterostructures without the need for a forming step and with resistance values that could be continuously varied over two orders of magnitude [38]. The L2NO4's oxygen content (in the form of interstitial point defects) affects both its structure and electrical properties and was shown to play a crucial role in the memristive response of these devices [42]. Furthermore, this MIEC material was also combined with a bottom perovskite film, forming $LaNiO_3/La_2NiO_4$ bilayer planar devices (using Pt electrodes) [43]. This original device design showed interesting memristive properties, which were strongly affected by the film microstructure and oxygen content, which strongly depended on the oxygen partial pressure used during the pulsed-laser deposition of each of the layers.

Recently, the previously mentioned L2NO4 planar memristive devices were successfully transferred to vertical Ti/L2NO4/Pt structures [39]. Nevertheless, these devices still presented certain cycle-to-cycle (c2c) and device-to-device (d2d) variability and resistance relaxation with time. In addition, the pulsed mode operation, as well as the capacity of L2NO4-based devices to present LTP/LTD for their evaluation as ANN memristive elements is still missing. In this work, the growth of high-quality L2NO4 thin films on Pt substrate has been carried out using previously optimized parameters and used to construct L2NO4-

based devices using TiN as the top electrode for the first time. The TiN was chosen as an active electrode in this work due to its CMOS compatibility, relatively large work function and dry etching capabilities [18]. The active layer and the memristive devices were then structurally, chemically and electrically characterized. We present the memristive properties of such devices, which allow for better control of the c2c and d2d variability compared to the Ti-electrode-based devices, in addition to LTP/LTD characteristics suitable for artificial synapse applications. What is more, the behavior of these novel TiN/L2NO4/Pt devices was tested in a Spiking Neural Network (SNN) with online learning, resulting in a high system-level accuracy for optimized pulse voltage and duration combinations.

2. Experimental section

Polycrystalline $La_2NiO_{4+\delta}$ films were deposited on 1x1cm^2 substrates which consist of Pt (100 nm)/TiO_2 (20 nm)/SiO_2 (500 nm)/Si (750 µm)/SiO_2 (500 nm) from top to bottom, supplied by CEA-Leti. The L2NO4 thin films were synthesized by pulsed injection – metal organic chemical vapor deposition (PI-MOCVD) [44,45]. $La(tmhd)_3$ (tris(2,2,6,6-tetramethyl-3,5-heptanedionato)lanthanum(III)) and $[Ni(tmhd)_2]$ (bis(2,2,6,6-tetramethyl-3,5-heptanedionato)nickel(II)) precursors from Strem Chemicals were mixed in a 0.02 M solution with m-xylene (1,3-dimethylbenzene) from Alfa Aesar. The L2NO4 growth conditions used in this work are detailed in Table 1 and correspond to the optimized deposition conditions for L2NO4 thin films grown on Pt [39].

Table 1: Parameters used for the deposition of L2NO4 thin films by PI-MOCVD

Parameters	Value
Injection frequency	1 Hz
Opening time	2 ms
Number of pulses	2000
Evaporation temperature	220 - 280°C
Substrate temperature	600°C
Carrier gas	218 sccm (34% Ar) + 418 sccm (66% O_2)
Total pressure inside the reactor	5 Torr

For the phase identification of the L2NO4 thin films, X-ray diffraction in grazing incident mode (GI-XRD) was carried out in a 5-circle Rigaku Smartlab diffractometer. The surface morphology was studied by scanning electrode microscopy (SEM) in an SEM FEG ZEISS GeminiSEM 300 microscope. The surface roughness was investigated by atomic force microscope (AFM) in an AFM D3100 Veeco Instrument in tapping mode with a Si_3N_4 tip probe. Morphological and elemental characterization was performed by transmission electron microscopy (TEM) in an FEI Tecnai OSIRIS, working at 200kV and equipped with the SuperX EDX system. For this purpose, TEM lamellas were prepared by Focus Ion Beam (FIB) using an FEI Helios DualBeam FIB operating at 30 kV.

The microfabrication of the devices was carried out in the PTA clean-room facilities (Grenoble), including laser lithography (Heidelberg instrument µPG 101) and TiN deposition by reactive sputtering equipment (PVD 100 Alliance Concept, the deposition rate is 0.2 nm/s).

The current-voltage measurements were carried out on TiN/L2NO4/Pt devices using a Keithley 4200 semiconductor parameter analyzer in sweep mode and pulse modes using a source measurement unit and pulse measurement unit, respectively, and two external micromanipulators. The voltage was applied at the top TiN electrode while the bottom Pt electrode was grounded. In sweep mode, the bipolar triangular voltage sweeps always follow the sequence: 0 V → $+V_{max}$ → 0 V → $-V_{max}$ → 0 V, with the step of 0.01 mV. After each half cycle (0 V → $+V_{max}$ → 0 V or 0 V → $-V_{max}$ → 0 V), a sweep (0 V → 0.01 V) was applied to readout the resistance. The current compliance was set at 100 mA at the negative branch to avoid the device breakdown. The resistance state was read by measuring the current at 0.01 V (reading test: 0 V → +0.01 V). For high-temperature retention measurements, the device was baked at the temperature of 85 °C for 30, 60, 90, 120, 150 and 180 min using a 1/2″ ceramic heating stage in a high-temperature cell (Nextron). The surface temperature of the heater was calibrated beforehand using a Pt100 thermocouple. The resistance state was measured at RT in between baking by measuring the current at 0.1 V (reading test: 0 V → +0.1 V). In the pulse mode, the parameters used for the write and read pulses are varied depending on the tests and their range, which is detailed individually in the description of each test.

3. Results and discussion

3.1. Structural characterization of TiN/L2NO4/Pt memristive devices

The structure, microstructure and morphology of the L2NO4 thin films deposited on platinized substrates have been characterized by GI-XRD, SEM and AFM. Figure 1a shows the GI-XRD diffraction pattern of the L2NO4/Pt sample. The Pt diffraction peaks are marked by gray circles. The rest of the main diffraction peaks can be assigned to either the tetragonal phase *I4/mmm* (ICDD: 00-034-0314, presented at the bottom) or the orthorhombic phase *Fmmm* (ICDD: 01-086-8663, presented at the top) of $La_2NiO_{4+\delta}$. The patterns of both structures are very similar and, therefore, it is extremely difficult to discriminate between them based on GI-XRD exclusively. However, it can be seen that all the films are polycrystalline, confirmed by the match of the peak positions between the L2NO4/Pt sample and those of the database plotted by drop lines in Figure 1a. The surface morphology of the L2NO4 film was analyzed by SEM and AFM. As can be seen from Figure 1b the thin film is dense, homogeneous and formed by small grains (average size of 23.4 nm). The AFM image confirms that the film is flat with an RMS (root mean square) value of 3.4 nm (Figure 1c).

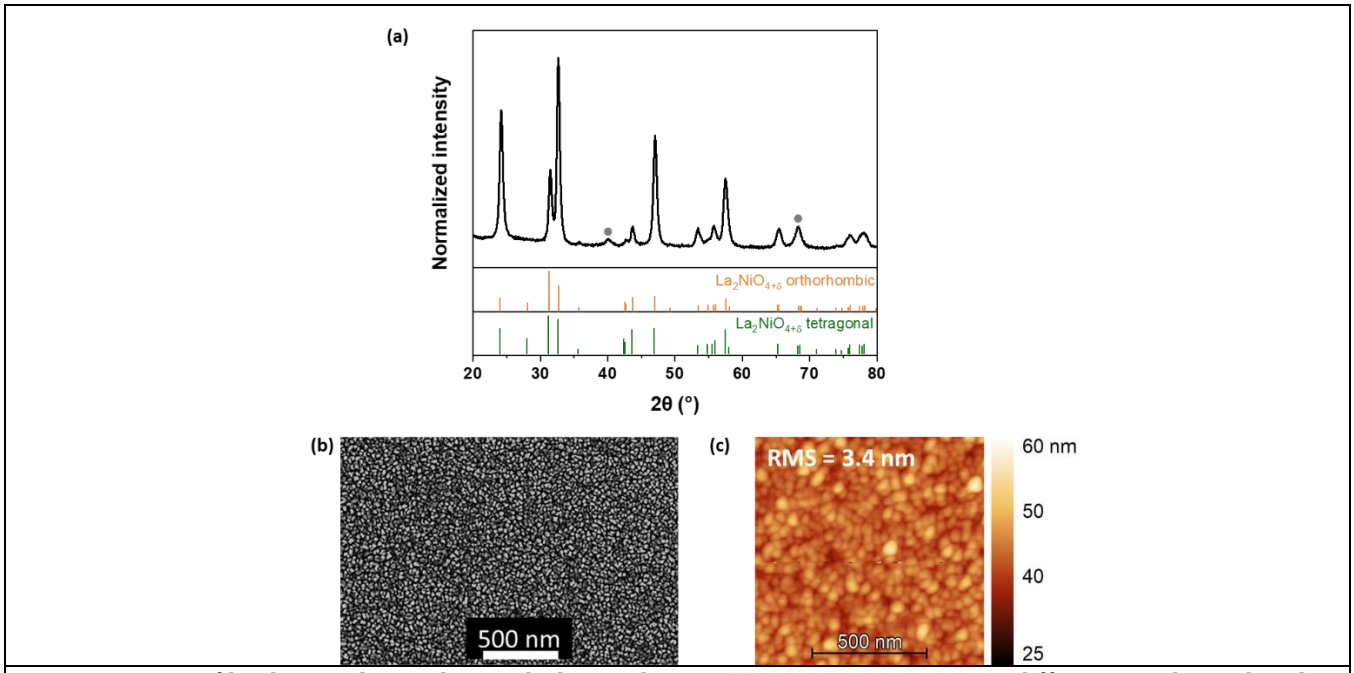

Figure 1. L2NO4 film deposited on a platinized silicon substrate: (a) GI-XRD pattern, main diffraction peaks attributed to the either $La_2NiO_{4+\delta}$ tetragonal phase (space group *I4/mmm*; ICDD: 00-034-0314; green lines at the bottom) or the orthorhombic phase (space group *Fmmm*; ICDD: 01-086-8663; orange lines at the bottom) in polycrystalline form (randomly oriented). The presence of Pt peaks is marked by their orientations (ICDD: 04-001-2680) and is indicated by the gray dots. (b) SEM image and (c) AFM image of the sample surface.

The microfabrication of TiN electrodes was then performed to construct the memristive devices. A device in the pristine state prior to any electrical measurements was chosen to prepare a lamella for TEM observations. Figure 2a shows the STEM image of the TiN/L2NO4/Pt lamella, showing that the L2NO4 film and TiN layer are continuous and dense. A thickness of 33.8 ± 1.7 nm was measured for the L2NO4 film. The EDX elemental maps (Figure 2Figure b) and EDX depth profile (Figure 2c) show that the complete stack is composed of well-defined layers separated by sharp interfaces as follows (from top to bottom): the TiN top electrode, the L2NO4 switching layer, the Pt bottom electrode and the TiO_2 adhesion layer underneath. A uniform distribution of the La, Ni and O elements is observed within the L2NO4 thin film. No element diffusion between these three layers is observed, except for a small amount of oxygen detected at the bottom part of the TiN electrode (distance of around 70 nm in Figure 2c). It is worth emphasizing that the lamella of the device was taken in the as-fabricated state prior to any electrical measurements. Therefore, the presence of oxygen at the TiN/L2NO4 interface suggests it is likely a TiN_xO_y interlayer (approximately 3 nm) which is spontaneously formed during the evaporation of TiN. The presence of a TiN_xO_y interlayer has been previously reported in other oxide memristive systems using TiN as an oxidizable electrode [46,47].

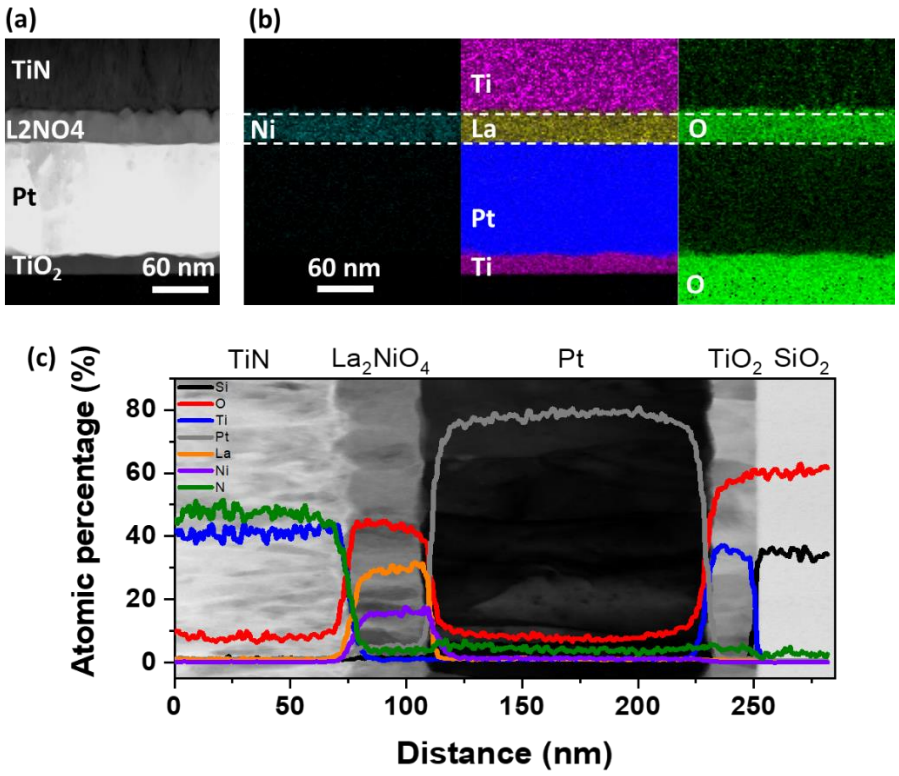

Figure 2: Cross-section TEM analysis of a pristine (as-fabricated) TiN/L2NO4/Pt memristive device: a) STEM image showing the layer stack of the device, b) EDX elemental maps for Ti (pink), La (yellow), Pt (blue), Ni (cyan) and O (green), c) EDX atomic depth profile showing a small amount of oxygen at TiN/L2NO4 interface.

3.2. Electrical characterization of TiN/L2NO4/Pt memristive devices

Figure 3 shows the typical RS behavior of the TiN/L2NO4/Pt memristive device. At the first application of positive bias, the device is in the intermediate resistance state (IRS) with the mean value of ~20 kΩ calculated over 10 measured devices. Next, at the first cycle of the $|V_{max}|$ = 2.5 V sweep, a sudden increase in current occurs at the negative polarity, reaching current compliance, which is considered as a 'soft-forming' of the devices due to the lack of current overshoot and small but rapid change in current (Figure 3a). Figure 3b presents every 20th IV sweep from 200 consecutive sweeps at $|V_{max}|$ = 2.5 V after the "soft-forming" occurs, showing a counter eightwise RS for the TiN/L2NO4/Pt memristive devices with an HRS/LRS ratio of ~37. Gradual transitions between the HRS and LRS occur both for the RESET and SET operations, suggesting that bipolar analog RS can be obtained on TiN/L2NO4/Pt memristive cells. The presence of a "soft-forming" step implies that a conductive filament (CF) was created in the device (filamentary RS mechanism). Another indication of the presence of a CF is the independence of HRS and LRS from the device's area (inset in Figure 3b). The "soft-forming" step is different from the conventional forming step usually observed in the other oxide-based VCMs due to: i) the lack of current overshoot; ii) a small but rapid change in current; iii) the same voltage range as for the following sweeps; and iv) LRS resistance in the kΩ range. The presence of the "soft-forming" at the same voltage as the standard RS rather than the conventional forming at the much higher voltage is one of the advantages of our system in comparison to other materials where filamentary RS is usually observed, for example, HfO_2 [48] or TaO_x [49], since it allows to simplify the circuit design and the testing protocol.

As shown by TEM and EDX measurements (Figure 2), the formation of the TiN_xO_y interlayer of ~ 3 nm thickness occurs at the TiN/L2NO4 interface due to the oxygen interstitials inside the L2NO4 layer. We believe that the formation of the CF consisting of oxygen vacancies could occur in the TiN_xO_y interlayer since it is expected to be nonstoichiometric. Simultaneously, L2NO4 would act as an oxygen reservoir layer. During the application of a positive bias to the TiN electrode, oxygen ions from the L2NO4 layer would drift towards the TiN_xO_y interlayer and the CF is ruptured which leads to HRS.

Conversely, at negative polarity, oxygen ions would move back to the L2NO4 layer and the CF is formed again, leading to LRS (Figure 3c).

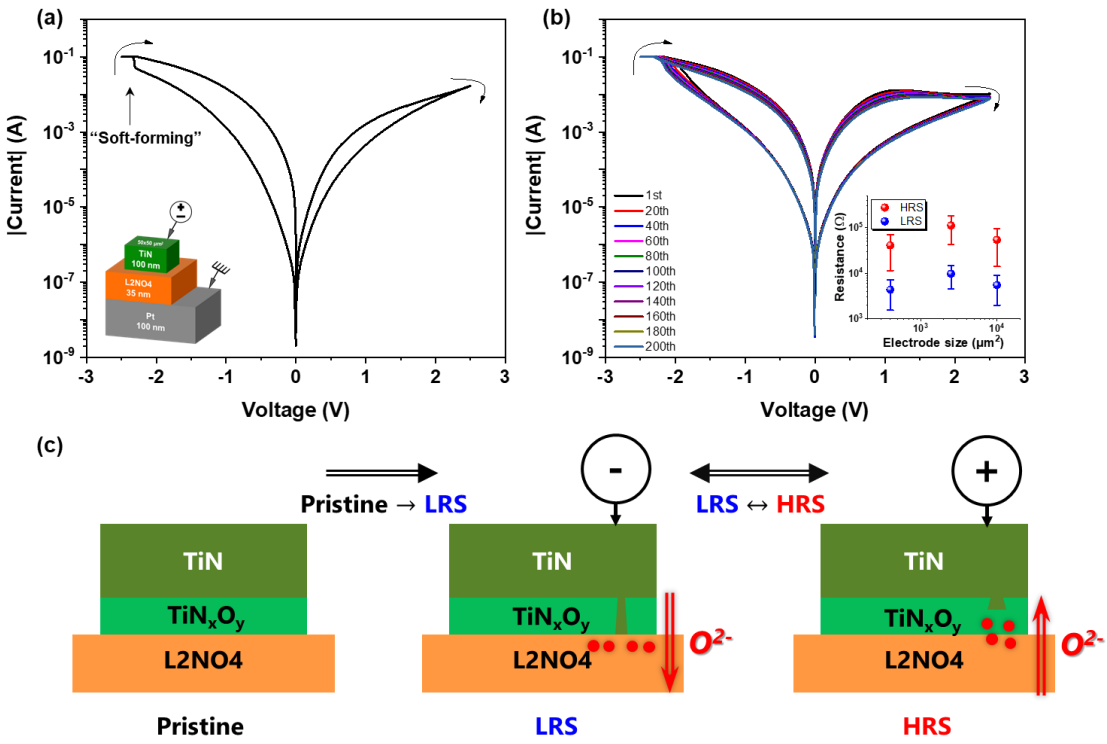

Figure 3. The IV characteristics of the TiN/L2NO4/Pt device corresponding to (a) the first cycle (after the first application of the bias) and (b) the regular cycling with 200 consecutive sweeps (every 20th sweep is shown). The inset shows the electrode size area independence resistance of the HRS (red) and LRS (blue). (c) The schematic image of the proposed RS mechanism in the TiN/L2NO4/Pt structures. Firstly, a CF is formed in the TiN_xO_y layer during the "soft-forming" process. During the application of the positive bias to the TiN electrode, the oxygen ions from the L2NO4 layer drift towards the TiN_xO_y layer and the CF is ruptured, which leads to HRS. In reverse, at the negative polarity, the oxygen ions move back to the L2NO4 layer and the CF is formed again which leads to LRS.

A common issue for filamentary memristive devices is a cycle-to-cycle (c2c) and device-to-device (d2d) variability that is related to the stochastic nature of the CF formation [13,50,51]. To investigate the variability of the TiN/L2NO4/Pt device, we performed cumulative probability (CP) calculations. Figure 4a shows the CP plot for the c2c variability based on 256 convective IV sweeps for a single device. It can be seen that the device shows outstanding c2c variability of HRS, with the standard deviation (σ) being only 4 %. However, in the LRS the device is more volatile, with σ = 15 %. Next, the d2d variability was analyzed based on the data from 30 devices with 5-10 IV sweeps for each device (Figure 4b). The σ value of the resistance in LRS and HRS was found to be 67% and 78%, respectively. It can be seen that the d2d variability is significantly higher than c2c, which can be attributed to the variations in the CF formation process in different devices [50]. The L2NO4 film roughness (Figure 1c) can also contribute to the d2d variability.

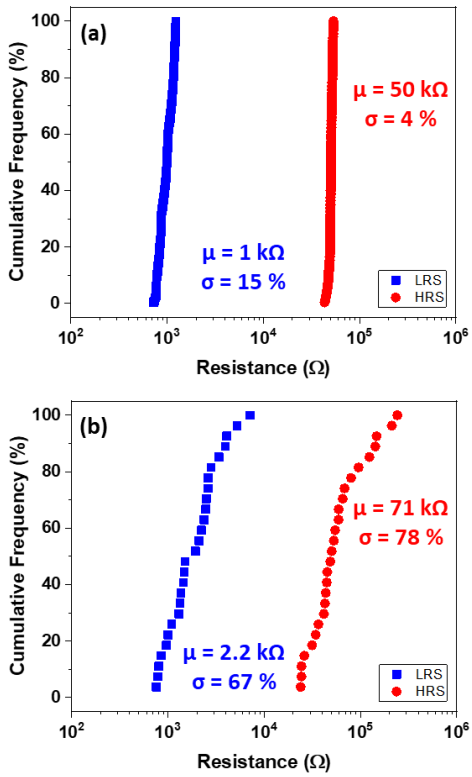

Figure 4. Statistical distributions of R_{LRS} and R_{HRS} for the TiN/L2NO4/Pt device. (a) Cycle-to-cycle variability measured from 1 device with 256 DC sweeps. (b) Device-to-device variability measured from 30 devices with mean R values for each device. V_{READ} = 0.1 V

The endurance of the TiN/L2NO4/Pt devices was measured by the application of a train of pulses, which allows for studying the behavior of the device from the perspective of the technological application (Figure 5a). In this test, the device was switched between the HRS and LRS using single pulses of 10 µs duration, with constant voltages for V_{SET} = -3.2 V and V_{RESET} = 2.8 V. It can be observed that the RS process takes place even with the application of pulses in the µs range. However, the memory window is much smaller compared to the one extracted from the IV characteristics (HRS/LRS ratio ~ 3). The distinguishable HRS and LRS could be observed throughout the pulse endurance test, however, the memory window starts decreasing after ~$5x10^4$ switching cycles. Figure 5b shows the comparison between the IV characteristics of the device before cycling and the cycled device after 10^4 and 10^5 cycles. Even though a certain memory window degradation is observed in the pulse regime, the IV characteristics remain quite stable after cycling, even after 10^5 pulses. Therefore, we can conclude that the endurance of the device in the pulse regime is of about $5x10^4$ switching cycles, after which a memory window degradation is observed.

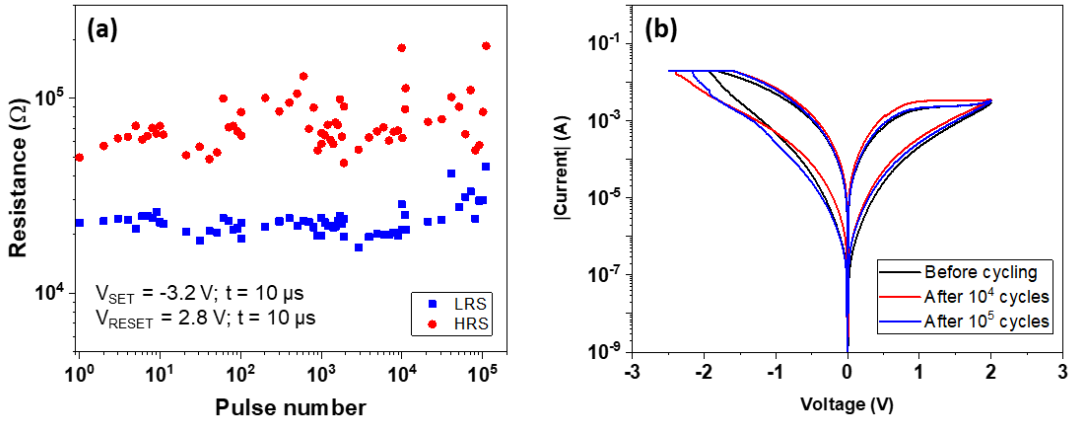

Figure 5. (a) Endurance test results for the TiN/L2NO4/Pt memristive device. (b) The IV characteristics of the TiN/L2NO4/Pt device obtained before the endurance test and after 10^4 and 10^5 switching cycles.

To evaluate the retention characteristics, a device was programmed to HRS (40 kΩ) by a half-cycle voltage sweep (0 V → +2.5→ 0 V). The HRS was then measured (every 5 minutes) for 6 hours at room temperature (RT) by a read test. Next, an LRS of 0.7 kΩ was programmed by a half cycle of a voltage sweep (0 V → -2.5→ 0 V) and was then measured for 6 hours, using the same read test as for the HRS. The evolution of the HRS and LRS vs time (t) is shown in Figure 6a. The HRS state value slightly increased during 6 hours of the measurement, starting from 37.2 kΩ to 40.7 kΩ, while a very small relaxation (a slight increase from 750 Ω to 800 Ω) of the LRS was observed during the first 45 minutes of the measurements, and stayed stable until the end of the test. Hence, a very good differentiation of the two resistance states (HRS/LRS ratio of 50 at t = 0 h and 51 at t = 6 h) was maintained for the 6h of the measurement. Furthermore, it was also possible to program the device to different resistance states by using pulses of different amplitude. Figure 6b shows four distinguishable resistance levels and their evolution with time (during 15 minutes), showing good retention after a slight resistance increase for the HRSs programmed at the highest voltages (+2.25 V and +2.5 V).

To verify the non-volatile properties of the TiN/L2NO4/Pt device, we conducted the retention measurement at an elevated temperature. For this test, we programmed 3 devices in LRS and 3 devices in HRS by application of a half-cycle voltage sweep (0 → V → 0) in the negative and positive polarity, respectively, and then kept the devices at 85 °C to facilitate the degradation of the resistance. The resistance of the devices was measured every 30 min at RT in between baking at V_{READ} = 0.1 V. The LRS and HRS resistance values shown in Figure 6c are averaged over the 3 devices at each state, showing that at 85 °C, the resistance of the TiN/L2NO4/Pt device stabilizes after ~ 1 hour of baking at ~ 4 kΩ for LRS and ~ 65 kΩ for HRS, with the HRS/LRS ratio being ~16. These results indicate good data retention characteristics and, thus, the suitability of using TiN/L2NO4/Pt as a non-volatile memory.

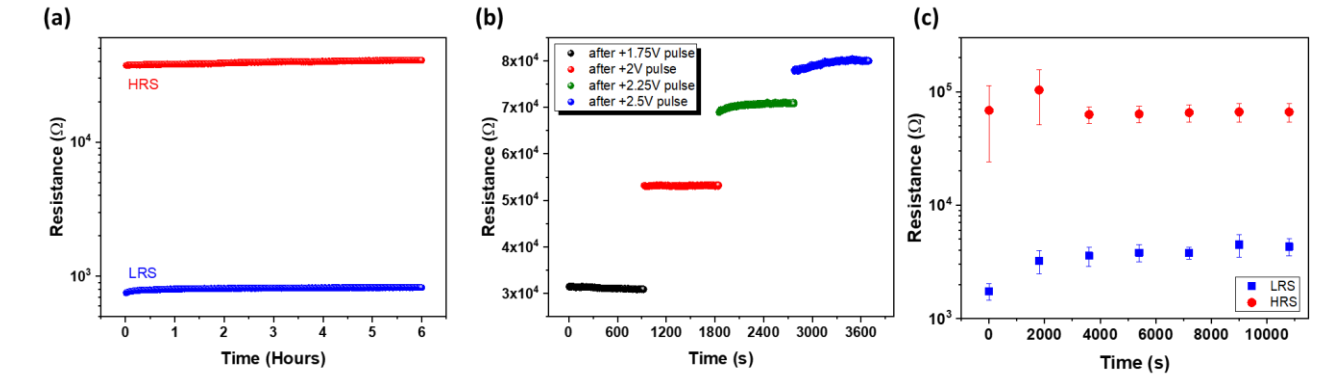

Figure 6. Retention characteristics of a TiN/L2NO4/Pt memristive device measured for (a) 6 hours after programming the HRS and LRS by half-sweeps of $|V_{max}|$ = 2.5 V and for (b) 15 minutes at RT. Four different resistance states programmed by pulses of 250 ms for pulse amplitudes of +1.75 V, +2.00 V, +2.25 V, +2.5 V. (c) Retention characteristics of a TiN/L2NO4/Pt memristive device measured every 30 min at RT in between baking at 85 °C for 3 hours (>10^4 s).

3.3. Analog properties of TiN/L2NO4/Pt memristive devices

Gradual resistive switching observed in the TiN/L2NO4/Pt device (Figure 3b) allows for the achievement of multiple resistance states, which is necessary to emulate the synaptic plasticity effect. To further assess the analog properties of the device, the DC multi-states modulation was analyzed, with the control of the SET process by the application of different current compliance and the RESET process by the application of different voltage amplitude. Figure 7 shows multiple resistance levels reached during the gradual RESET and SET processes. The measurements were carried out by the consecutive increase of the RESET voltage in the positive polarity region (0 → V_{RESET1} → 0 → V_{RESET2} → 0… → V_{RESET8} → 0.) The gradual SET process was demonstrated with the application of current compliance varied at the negative polarity from -10^{-4} A to -2×10^{-2} A. For a more convenient interpretation, Figure 7 contains the numbers of the curves in the order they were obtained. It can be seen that a gradual increase in the V_{RESET} leads to a gradual decrease in the HRS current, allowing one to get multiple discrete HRS levels. At the same time, positive current compliance alteration allows us to achieve multiple discrete LRS levels. A total of 16 different resistance states in the range from ~1 kΩ to ~181 kΩ were achieved. The inset shows the resistance levels measured at V_{READ} = 0.1 V on the backward voltage sweep (V → 0). Therefore, the device demonstrated analog properties required for the potential neuromorphic applications.

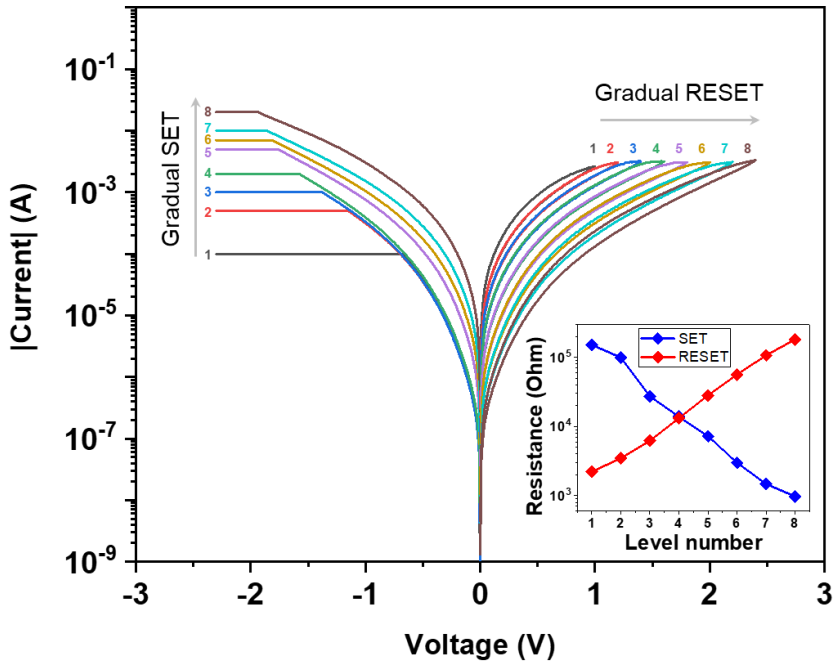

Figure 7. Analog IV characteristics of the TiN/L2NO4/Pt device: different resistance states obtained by the current compliance increase in the negative polarity and by the RESET voltage increase in the positive polarity. Inset shows the resistance levels achieved with the gradual SET and RESET processes measured at V_{READ} = 0.1 V on the backward voltage sweep (V → 0).

For use as non-volatile memories and for their application as artificial synapses, where the synaptic weight (conductance) is controlled by spikes, pulsed input signals are usually preferred. To this end, measurements using pulses were carried out to study the responses of the TiN/L2NO4/Pt memristive devices (Figure S2 in the Supplementary material). A staircase of write pulses was applied, followed by consecutive read pulses, following the so-called resistance hysteresis switching loop (RHSL) test. The IV values obtained by RHSL measurement (Figure S3a in the Supplementary material) were found to be perfectly consistent with the I-V measurements in continuous IV sweep mode, further confirming that the TiN/L2NO4/Pt memristive device can be used in both modes (pulse and sweep). Figure S3b in the Supplementary material presents the resistance window taken from the read pulses. The obtained HRS/LRS ratio is 35, which is comparable to that of continuous sweeps in Figure 3b. Moreover, multiple intermediate states can be measured between both extremes. These results show stable responses of TiN/L2NO4/Pt memristive devices under pulse input and confirm the reproducibility of the switching with multiple intermediate resistance states. The RHSL test also shows that a high linearity of the weight update curve can be achieved by the application of the pulse train with a gradual increase of the voltage amplitude. Figure 8a shows the data extracted from the rising edge of the curve in Figure S3b in the range from 0.25 V to 2.5 V for depression and from -0.25 V to -2.5 V for potentiation. It can be seen that a close to linear resistance update is observed in the range from 1.5 V to 2.5 V for depression. On the other hand, for potentiation, the resistance changes linearly almost in the whole investigated range (from -0.25 V to -2.25 V). The high linearity of weight update in response to the gradually increasing pulse train was also reported in previous studies for other memristive devices [52,53]. However, in a neural network, the integration of non-identical spikes leads to over-complication of the circuit design, therefore, the use of identical spikes is preferred [54]. In addition, it has been previously reported that the SNNs have a strong tolerance for the device's non-linearity and keep the accuracy high for a wide range of non-linearity factors [55].

To study the suitability of TiN/L2NO4/Pt devices as artificial synapses with the pulse trains of fixed amplitude (Figure S4 in the Supplementary material), the LTP/LTD measurements were performed using different pulse amplitude combinations between +1.25 V and +2 V for the positive pulses and between -0.75 V and -1.25 V for the negative pulses. Fifty (or one hundred) consecutive identical positive pulses (for LTP) were followed by fifty (or one hundred) identical negative pulses (for LTD). Non-linear asymmetric LTP/LTD curves were obtained in all cases, as shown in Figure 8b for the sequence of depression pulse [+2.00 V; 250 ms], potentiation pulse [-1.25 V; 250 ms] and read pulse [0.1 V; 50 ms]. Further results using different

voltage amplitudes and number of pulses are shown in Figure S5 in the Supplementary material. In all cases, the device resistance increased when applying repeatedly positive pulses and decreased when applying negative pulses. The resistance change is larger for the first LTP and LTD pulses, and gradually smaller for the last pulses at the end of each sequence. In addition, a steep jump from HRS with the first pulse is observed for LTP. We believe that the application of a single pulse with high voltage amplitude V_{max} induces a steeper change in the device's chemistry than the application of the DC sweep where the voltage is gradually increased from 0 to V_{max}. In addition, in the filamentary mechanism, it is typical to have gradual RESET but abrupt SET [23]. These LTP/LTD measurements indicate that the potentiation/depression characteristics observed in biological synapses can be artificially performed in the TiN/L2NO4/Pt memristive devices.

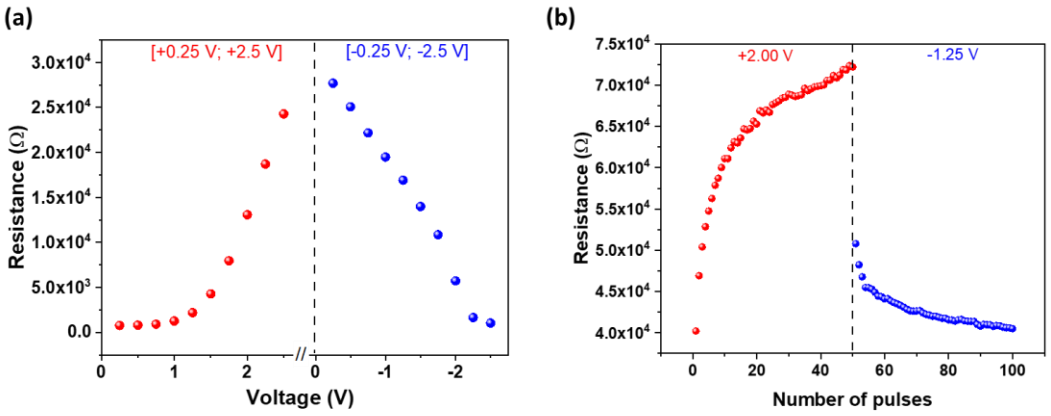

Figure 8. Evolution of resistance in TiN/L2NO4/Pt memristive devices as (a) a function of the voltage (depression/potentiation tests with gradually increasing voltage amplitude) and (b) a function of the number of pulses (depression/potentiation tests with fixed amplitude). The duration of the write and read pulses was 250 ms and 50 ms, respectively, for both tests.

The effect of pulse duration was studied by three depression measurements of different durations, which results are plotted in Figure 9a. The voltage amplitude was fixed at +2.5 V. As can be observed, the longer the pulse duration, the higher the resistance value obtained at each n^{th} pulse. The values included in Figure 9a are replotted in Figure 9b as the resistance as a function of the total applied pulse duration showing a continuous behavior. This result suggests the total change in resistance strongly depends on the total applied time of the pulses, and not on the total number of individual pulses. These results prove that, by combining different pulse amplitudes and pulse durations, the resistance of TiN/L2NO4/Pt memristive cells can be controlled and programmed flexibly.

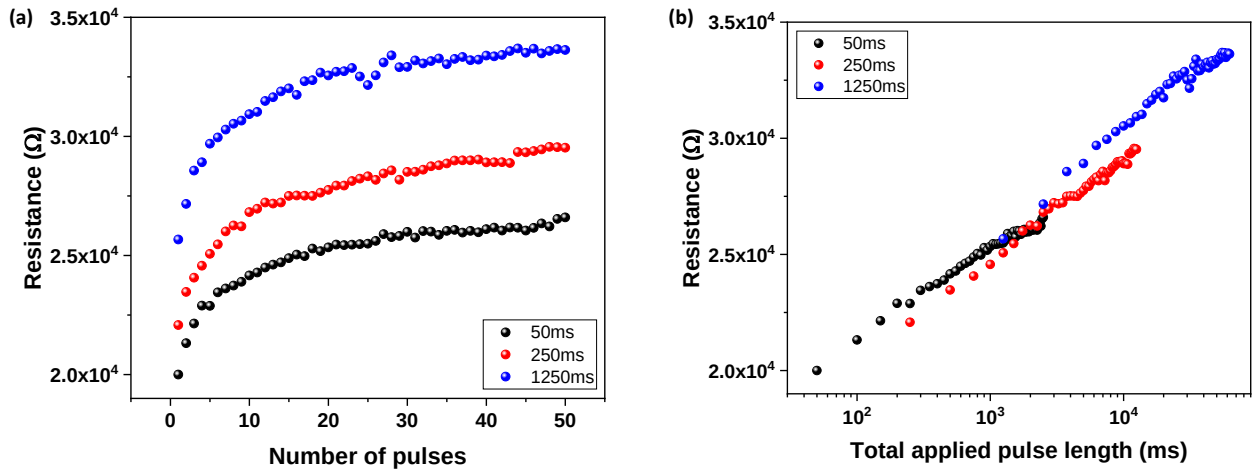

Figure 9: a) Depression measurements on TiN/L2NO4/Pt memristive devices using three different pulse durations: 50, 250 and 1250 ms. b) Resistance of the depression measurements plotted as a function of the total applied pulse duration. The write voltage amplitude of Vmax = +2.5 V was applied in all cases.

3.4. L2NO4-based memristors in Spiking Neural Networks (SNNs) with on-line learning

To verify and validate the behavior of the proposed L2NO4-based memristors in terms of system-level accuracy their behavior in a Spiking Neural Network (SNN) with on-line learning was evaluated. The purpose of this study is to demonstrate that the electrical characteristics of the device under study can be effectively used for training a neural network online, in an unsupervised fashion. For this study, we have used an in-house computation tool that emulates, at the functional level, the behavior of a fully connected SNN with leaky-integrate and fire neurons and spike-timing-dependent synaptic plasticity (STDP). The tool [56] is built for the MNIST database and allows for the customization of neuron and synapse models as well as the network size. The implemented algorithm is based on the work of Diehl and Cook [57], further optimized to allow for fast execution times and full flexibility regarding the synaptic trace during the training process. The functionality of the tool and its data structure are illustrated in Figure 10a and Figure 10b respectively. The in-house simulator allows simulation of the full behavior of an SNN with STDP while minimizing the execution time. Its operation can be briefly described as follows. The input data is converted in a spike pattern via spike coding (rate coding following Poisson distribution, in this particular case), each generated spike being defined by the time it occurs and the corresponding input position within the network. The spike is propagated through the corresponding synapses and the value of the weight is added to the related output neuron ($out = \sum d(W)$). When the accumulator of an output neuron crossed the threshold, it generates the output spike. In this instant (i) the lateral inhibition is activated and all other output neurons are inhibited (ii) the weights of all the synapses connected to the output neuron that spiked are updated. This update is executed according to $\Delta W = f(\delta C)$, δC as the memristive conductance increment or reduction defined for synaptic potentiation or depression, and f as the function that governs the memristive conductance variation, i.e., the synaptic plasticity function. In this study, the synaptic plasticity function is extracted from the memristor behavior illustrated in Figure 8b and Figure S5 by fitting the measured data to the asymmetric conductance model [58]. For this preliminary study, since no assumption can be yet made on the synaptic control hardware, we have chosen to use for the synaptic update during training the simplified STDP rule, which states that (i) if an output spike occurs immediately after an input spike (with a maximum delay δt between the two spikes), the synapse will be potentiated, i.e., its weight value will increase by a constant factor W+; (ii) if the delay between the output spike and the input spike is larger than δt, the synapse will be depressed, i.e., its weight value will decrease by a constant factor W-. The W+ and W- are commonly known as LTP and LTD respectively. To avoid biasing the results due to fitting errors we modified our tool to extract the LTP and LTD values at each synaptic update from a lookup table which stores the conductance values extracted from the electrical measurements for both potentiation and depression. Therefore, synaptic weights are initialized to random values extracted from this lookup table and the synaptic values are updated during training according to the simplified STDP rule. The main data structures can be described as follows: *inN*: represents the set of inputs, for each input the time when the last spike occurred is stored (*lastSpike*); *spike*: it is an array that contains the list of input spikes to be processed; *outN*: represents the set of output neurons. For each neuron, we store: the accumulator (a variable storing the quantity of information arriving at the output neuron); the inhibition (a variable storing the information of the duration for which the neuron is inhibited); *the lastSpike* (the time when the last spike occurred to calculate the STDP function); *S*: this matrix contains the values of the weight of every single synapse.

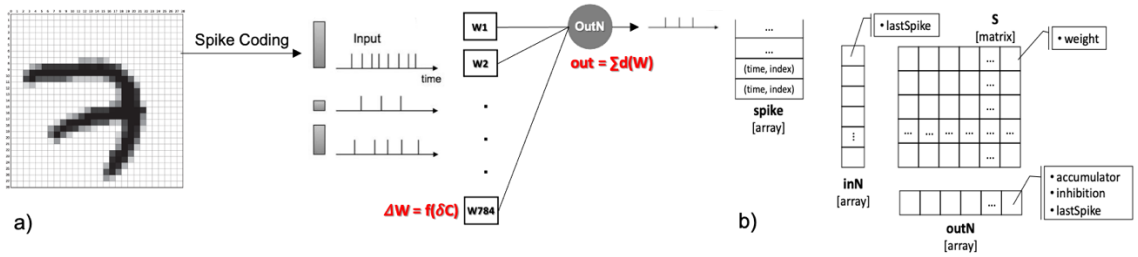

Figure 10. Simulator of an SNN with STDP a) Schematic representation of the operation principle. b) Data-structure.

The in-house tool has been used to estimate the usability of the proposed L2NO4-based memristive devices as synapses for an SNN with STDP designed to solve the MNIST [59] database of handwritten digits. The MNIST datatabase has been chosen for simplicity, any other SNN-compatible dataset could be theoretically used in this study. This database has $6x10^4$ examples for network training and 10^4 examples for testing the network. Each example is the image of a hand-written digit with 28x28 pixels in greyscale (256 tones of grey from white to black). The information carried by each image is transmitted to the network in the form of spikes. The spike encoding is performed by frequency encoding of each pixel's tone of grey. Each image is presented to the network for 10 time units. Therefore, the network has 784 inputs (one per image pixel), 300 output neurons

and 235200 synapses (as the network is fully connected, i.e., a synapse exists between any pair of input-output). The accuracy of the network is estimated for different configurations of the control signals (illustrated in Figure 10) and the results obtained for the three best combinations of pulses are summarised in Table 2. It should be noted that the network accuracy depends on the characteristics of the control signals, with maximum obtained accuracies between 73 and 78%. These results validate the compatibility of the proposed L2NO4-based memristive devices with the STDP training. It should be noted that the base accuracy for the SNN under study is 86% as reported by Diehl and Cook at the algorithmic level [57]. Therefore, by using a simplified learning rule and raw data extracted from electrical measurements, we observe an accuracy loss of 8% compared with the maximum accuracy allowed by algorithm.

Table 2: Accuracy estimation of an L2NO4-based SNN trained using STDP for MNIST database (base accuracy of the tool under ideal conditions 86%)

Signal amplitude during depression/potentiation	Accuracy
$+V_{max}$ = +2.0 V, $-V_{max}$ = -1.25 V (Figure 8b)	76.8%
$+V_{max}$ = +1.5 V, $-V_{max}$ = -1.0 V (Figure S5)	78.0%
$+V_{max}$ = +1.25 V, $-V_{max}$ = -0.75 V (Figure S5)	73.5%

To compare our devices to the state-of-the-art memristors, we analysed the works that implement inorganic perovskite-based memristive devices as artificial synapses in different types of ANN. Amongst perovskite oxides, the most researched material for neuromorphic computing is $Pr_{1-x}Ca_xMnO_3$ (PCMO). In addition, there are several studies on the perovskite halide memory devices such as $CsPbBr_3$ or $CsSnCl_3$. We summarized the synaptic properties of inorganic perovskite memristors as well as their test with neural networks and the achieved accuracy (if applicable) in Table 3.

Table 3. Comparison of the synaptic properties of the inorganic perovskite based memristive devices.

Material	**Number of DC analog states**	**LTP and LTD voltage/pulse duration**	**Network test**	**Dataset**	**Accuracy**	**Ref.**
$CsPbBr_3$	-	0.5 V – 2 V / 1 s	CNN	MNIST	96.7 %	[60]
$CsSnCl_3$	7	1.3 V / 10 µs	-	-	-	[61]
PCMO	12	2 V – 3 V / 10 ms	ANN	MNIST	97 %	[62]
PCMO	13	3 V / 1 ms	SNN	EEG/Cochlea	91.4 %	[54]
$La_2NiO_{4+\delta}$	16	0.75 V – 2.5 V / 250 ms	SNN	MNIST	78 %	This work

Following the comparison in Table 3, we would like to acknowledge that a convolutional neural network (CNN), for example, manages to solve the MNIST dataset with much higher accuracies than the ones we achieved in our work. However, for the CNNs, the training of the network is done offline by using backpropagation, while for SNN, unsupervised online learning is implemented. Although SNNs generally achieve lower accuracy (for example, the baseline accuracy in this work is 86%), they typically require much fewer operations and are better candidates for processing spatiotemporal data [6]. We want to note that in this work, we are not trying to demonstrate an advantage of SNNs over CNNs (or other networks) in terms of accuracy. Our focus is demonstrating that the proposed TiN/L2NO4/Pt devices can be used for unsupervised online learning (even before device optimization for STDP).

3. Conclusions

TiN/L2NO4/Pt vertical memristive devices with a polycrystalline L2NO4 switching layer have been fabricated on Si-based substrates for the first time. These L2NO4-based memristors show bipolar resistive switching with a gradual change in resistance during SET and RESET processes. In pulse mode, the resistance values can be finely tuned by using different pulse amplitudes or pulse durations. The device shows stable retention and endurance of ~$5x10^4$ switching cycles. The resistance of the TiN/L2NO4/Pt memristive devices, which can be regarded as the synaptic strength, is gradually tunable by the application of successive pulses of the same sign. The linearity of the weight update can be tuned by the application of gradually increasing pulse train, however, for SNN application, the use of the identical spikes is prefered as the SNN has strong tolerance for non-linearity. The resistance change with the application of the pulse train with the fixed pilse parameters strongly depends on the total applied pulse duration and on the voltage pulse amplitude, which can be finely tuned on desire. When tested in an SNN

environment, the device demonstrates good potentiation/depression behavior, allowing the online training of an SNN for MNIST which leads to 78% inference accuracy. These results prove that the TiN/L2NO4/Pt memristive device is a potential candidate for long-term artificial synapse applications for SNN.

Acknowledgments

This work was partially supported by the LabEx Minos ANR- 10-LABX-55-01 (for T.-K.K.), by ANR France within the EMINENT Project ANR-19-CE24-0001 and has also received financial support from the CNRS through the MITI interdisciplinary programs ("Synconnect" 80|PRIME project). This research has benefited from characterization equipment of the Grenoble INP–CMTC platform supported by the Centre of Excellence of Multifunctional Architectured Materials "CEMAM" n°ANR-10-LABX-44-01 funded by the "Investments for the Future" Program. Part of this work, carried out on the Platform for Nanocharacterization (PFNC), was supported by the "Recherches Technologiques de Base" program of the French National Research Agency (ANR). In addition, the work has been performed with the help of the "Plateforme Technologique Amont (PTA)" in Grenoble, with the financial support of the "Nanosciences aux limites de la Nanoélectronique" Fundation and CNRS Renatech network. The authors acknowledge Valentine Bolcato (PTA, Grenoble INP, France) for the deposition of the TiN layer and Céline Ternon (Grenoble INP, LMGP) for fruitful discussions.

Data availability

The data that support the findings of this study are available upon request from the authors.

References

[1] Mead C 1990 Neuromorphic electronic systems *Proceedings of the IEEE* **78** 1629–36

[2] Christensen D V, Dittmann R, Linares-Barranco B, Sebastian A, Le Gallo M, Redaelli A, Slesazeck S, Mikolajick T, Spiga S, Menzel S, Valov I, Milano G, Ricciardi C, Liang S-J, Miao F, Lanza M, Quill T J, Keene S T, Salleo A, Grollier J, Marković D, Mizrahi A, Yao P, Yang J J, Indiveri G, Strachan J P, Datta S, Vianello E, Valentian A, Feldmann J, Li X, Pernice W H P, Bhaskaran H, Furber S, Neftci E, Scherr F, Maass W, Ramaswamy S, Tapson J, Panda P, Kim Y, Tanaka G, Thorpe S, Bartolozzi C, Cleland T A, Posch C, Liu S, Panuccio G, Mahmud M, Mazumder A N, Hosseini M, Mohsenin T, Donati E, Tolu S, Galeazzi R, Christensen M E, Holm S, Ielmini D and Pryds N 2022 2022 roadmap on neuromorphic computing and engineering *Neuromorphic Computing and Engineering* **2** 022501

[3] Burr G W, Shelby R M, Sebastian A, Kim S, Kim S, Sidler S, Virwani K, Ishii M, Narayanan P, Fumarola A, Sanches L L, Boybat I, Le Gallo M, Moon K, Woo J, Hwang H and Leblebici Y 2017 Neuromorphic computing using non-volatile memory *Adv Phys X* **2** 89–124

[4] Lepri N, Glukhov A, Cattaneo L, Farronato M, Mannocci P and Ielmini D 2023 In-memory computing for machine learning and deep learning *IEEE Journal of the Electron Devices Society* 1–1

[5] Ielmini D, Wang Z and Liu Y 2021 Brain-inspired computing via memory device physics *APL Mater* **9** 050702

[6] Zhang Y, Wang Z, Zhu J, Yang Y, Rao M, Song W, Zhuo Y, Zhang X, Cui M, Shen L, Huang R and Joshua Yang J 2020 Brain-inspired computing with memristors: Challenges in devices, circuits, and systems *Appl Phys Rev* **7**

[7] Wang Z, Wu H, Burr G W, Hwang C S, Wang K L, Xia Q and Yang J J 2020 Resistive switching materials for information processing *Nat Rev Mater* **5** 173–95

[8] Ielmini D and Wong H-S P 2018 In-memory computing with resistive switching devices *Nat Electron* **1** 333–43

[9] Chen W, Song L, Wang S, Zhang Z, Wang G, Hu G and Gao S 2023 Essential Characteristics of Memristors for Neuromorphic Computing *Adv Electron Mater* **9** 2200833

[10] Dittmann R and Strachan J P 2019 Redox-based memristive devices for new computing paradigm *APL Mater*

[11] Bagdzevicius S, Maas K, Boudard M and Burriel M 2017 Interface-type resistive switching in perovskite materials *J Electroceram* **39** 157–84

[12] Dittmann R, Menzel S and Waser R 2021 Nanoionic memristive phenomena in metal oxides: the valence change mechanism *Adv Phys* **70** 155–349

[13] Baeumer C, Valenta R, Schmitz C, Locatelli A, Menteş T O, Rogers S P, Sala A, Raab N, Nemsak S, Shim M, Schneider C M, Menzel S, Waser R and Dittmann R 2017 Subfilamentary Networks Cause Cycle-to-Cycle Variability in Memristive Devices *ACS Nano* **11** 6921–9

[14] Koroleva A A, Kuzmichev D S, Kozodaev M G, Zabrosaev I V., Korostylev E V. and Markeev A M 2023 CMOS-compatible self-aligned 3D memristive elements for reservoir computing systems *Appl Phys Lett* **122**

[15] Koroleva A A, Kozodaev M G, Lebedinskii Y Y and Markeev A M 2021 Interface engineering for enhancement of the analog properties of W/WO 3− x /HfO 2 /Pd resistance switched structures *J Phys D Appl Phys* **54** 504004

[16] Koroleva A A, Kozodaev M G, Lebedinskii Y Y and Markeev A M 2021 Forming-Free Nonfilamentary Resistive Switching in W/WO3 – x/HFO2/Pd Structures *Nanobiotechnology Reports* **16** 737–44

[17] Zhang J, Wang F, Li C, Shan X, Liang A, Hu K, Li Y, Liu Q, Hao Y and Zhang K 2020 Insight into interface behavior and microscopic switching mechanism for flexible HfO2 RRAM *Appl Surf Sci* **526** 146723

[18] Yong Z, Persson K-M, Saketh Ram M, D'Acunto G, Liu Y, Benter S, Pan J, Li Z, Borg M, Mikkelsen A, Wernersson L-E and Timm R 2021 Tuning oxygen vacancies and resistive switching properties in ultra-thin HfO2 RRAM via TiN bottom electrode and interface engineering *Appl Surf Sci* **551** 149386

[19] Ryu J-H and Kim S 2020 Artificial synaptic characteristics of TiO2/HfO2 memristor with self-rectifying switching for brain-inspired computing *Chaos Solitons Fractals* **140** 110236

[20] Jonghan Kwon, Picard Y N, Skowronski M, Sharma A A and Bain J A 2014 In situ biasing TEM investigation of resistive switching events in TiO<inf>2</inf>-based RRAM *2014 IEEE International Reliability Physics Symposium* (IEEE) pp 5E.5.1-5E.5.5

[21] Banerjee W, Liu Q, Lv H, Long S and Liu M 2017 Electronic imitation of behavioral and psychological synaptic activities using TiO x /Al 2 O 3 -based memristor devices *Nanoscale* **9** 14442–50

[22] Kumari A, Shanbogh S M, Udachyan I, Kandaiah S, Roy A, Varade V and Ponnam A 2020 Interface-Driven Multifunctionality in Two-Dimensional TiO 2 Nanosheet/Poly(Dimercaptothiadiazole-Triazine) Hybrid Resistive Random Access Memory Device *ACS Appl Mater Interfaces* **12** 56568–78

[23] Koroleva A A, Chernikova A G, Chouprik A A, Gornev E S, Slavich A S, Khakimov R R, Korostylev E V., Hwang C S and Markeev A M 2020 Impact of the Atomic Layer-Deposited Ru Electrode Surface Morphology on Resistive Switching Properties of TaO x -Based Memory Structures *ACS Appl Mater Interfaces* **12** 55331–41

[24] Zhuk M, Zarubin S, Karateev I, Matveyev Y, Gornev E, Krasnikov G, Negrov D and Zenkevich A 2020 On-Chip TaOx-Based Non-volatile Resistive Memory for in vitro Neurointerfaces *Front Neurosci* **14** 1–8

[25] Yang J J, Zhang M-X, Strachan J P, Miao F, Pickett M D, Kelley R D, Medeiros-Ribeiro G and Williams R S 2010 High switching endurance in TaOx memristive devices *Appl Phys Lett* **97**

[26] Kuzmichev D S, Lebedinskii Y Y, Hwang C S and Markeev A M 2018 Atomic Layer Deposited Oxygen-Deficient TaO x Layers for Electroforming-Free and Reliable Resistance Switching Memory *physica status solidi (RRL) – Rapid Research Letters* **12** 1800429

[27] Prakash A, Jana D and Maikap S 2013 TaOx-based resistive switching memories: prospective and challenges *Nanoscale Res Lett* **8** 418

[28] Kubicek M, Schmitt R, Messerschmitt F and Rupp J L M 2015 Uncovering Two Competing Switching Mechanisms for Epitaxial and Ultrathin Strontium Titanate-Based Resistive Switching Bits *ACS Nano* **9** 10737–48

[29] Muenstermann R, Menke T, Dittmann R and Waser R 2010 Coexistence of filamentary and homogeneous resistive switching in Fe-doped SrTiO3 thin-film memristive devices *Advanced Materials* **22** 4819–22

[30] Meunier B, Pla D, Rodriguez-Lamas R, Boudard M, Chaix-Pluchery O, Martinez E, Chevalier N, Jiménez C, Burriel M and Renault O 2019 Microscopic Mechanisms of Local Interfacial Resistive Switching in LaMnO3+δ *ACS Appl Electron Mater* **1** 675–83

[31] Herpers A, Lenser C, Park C, Offi F, Borgatti F, Panaccione G, Menzel S, Waser R and Dittmann R 2014 Spectroscopic Proof of the Correlation between Redox-State and Charge-Carrier Transport at the Interface of Resistively Switching Ti/PCMO Devices *Advanced Materials* **26** 2730–5

[32] Moors M, Adepalli K K, Lu Q, Wedig A, Bäumer C, Skaja K, Arndt B, Tuller H L, Dittmann R, Waser R, Yildiz B and Valov I 2016 Resistive Switching Mechanisms on TaOx and SrRuO3 Thin-Film Surfaces Probed by Scanning Tunneling Microscopy *ACS Nano* **10** 1481–92

[33] Bagdzevicius S, Boudard M, Caicedo J M, Mescot X, Rodríguez-Lamas R, Santiso J and Burriel M 2019 Bipolar "table with legs" resistive switching in epitaxial perovskite heterostructures *Solid State Ion* **334** 29–35

[34] Bagdzevicius S, Boudard M, Caicedo J M, Rapenne L, Mescot X, Rodríguez-Lamas R, Robaut F, Santiso J and Burriel M 2019 Superposition of interface and volume type resistive switching in perovskite nanoionic devices *J Mater Chem C Mater* **7** 7580–92

[35] Park S, Chu M, Kim J, Noh J, Jeon M, Hun Lee B, Hwang H, Lee B and Lee B 2015 Electronic system with memristive synapses for pattern recognition *Sci Rep* **5** 10123

[36] Lashkare S, Chouhan S, Chavan T, Bhat A, Kumbhare P and Ganguly U 2018 PCMO RRAM for Integrate-and-Fire Neuron in Spiking Neural Networks *IEEE Electron Device Letters* **39** 484–7

[37] Khilwani D, Moghe V, Lashkare S, Saraswat V, Kumbhare P, Shojaei Baghini M, Jandhyala S, Subramoney S and Ganguly U 2019 Pr x Ca 1 − x MnO 3 based stochastic neuron for Boltzmann machine to solve "maximum cut" problem *APL Mater* **7**

[38] Maas K, Villepreux E, Cooper D, Jiménez C, Roussel H, Rapenne L, Mescot X, Rafhay Q, Boudard M and Burriel M 2020 Using a mixed ionic electronic conductor to build an analog memristive device with neuromorphic programming capabilities *J Mater Chem C Mater* **8** 464–72

[39] Khuu T, Lefèvre G, Jiménez C, Roussel H, Riaz A, Blonkowski S, Jalaguier E, Bsiesy A and Burriel M 2022 $La_2NiO_{4+\delta}$ -Based Memristive Devices Integrated on Si-Based Substrates *Adv Mater Technol* **7** 2200329

[40] Tarancón A, Burriel M, Santiso J, Skinner S J and Kilner J A 2010 Advances in layered oxide cathodes for intermediate temperature solid oxide fuel cells *J. Mater. Chem.* **20** 3799–813

[41] Burriel M, Téllez H, Chater R J, Castaing R, Veber P, Zaghrioui M, Ishihara T, Kilner J A and Bassat J-M 2016 Influence of Crystal Orientation and Annealing on the Oxygen Diffusion and Surface Exchange of La2NiO4+δ *The Journal of Physical Chemistry C* **120** 17927–38

[42] Maas K, Villepreux E, Cooper D, Salas-Colera E, Rubio-Zuazo J, Castro G R, Renault O, Jimenez C, Roussel H, Mescot X, Rafhay Q, Boudard M and Burriel M 2020 Tuning Memristivity by Varying the Oxygen Content in a Mixed Ionic–Electronic Conductor *Adv Funct Mater* **30** 1909942

[43] Maas K, Wulles C, Caicedo Roque J M, Ballesteros B, Lafarge V, Santiso J and Burriel M 2022 Role of pO2 and film microstructure on the memristive properties of La2NiO4+δ/LaNiO3−δ bilayers *J Mater Chem A Mater* **10** 6523–30

[44] Faucheux V, Pignard S and Audier M 2005 Growth of La2NiO4 thin films by chemical vapor deposition *J Cryst Growth* **275** e947–51

[45] Dubourdieu C, Roussel H, Jimenez C, Audier M, Sénateur J P, Lhostis S, Auvray L, Ducroquet F, O'Sullivan B J, Hurley P K, Rushworth S and Hubert-Pfalzgraf L 2005 Pulsed liquid-injection MOCVD of high-K oxides for advanced semiconductor technologies *Materials Science and Engineering: B* **118** 105–11

[46] Baek K, Park S, Park J, Kim Y-M, Hwang H and Oh S H 2017 In situ TEM observation on the interface-type resistive switching by electrochemical redox reactions at a TiN/PCMO interface *Nanoscale* **9** 582–93

[47] Meunier B, Martinez E, Rodriguez-Lamas R, Pla D, Burriel M, Boudard M, Jiménez C, Rueff J-P and Renault O 2019 Resistive switching in a LaMnO3 + δ/TiN memory cell investigated by *operando* hard X-ray photoelectron spectroscopy *J Appl Phys* **126**

[48] Matveyev Y, Egorov K, Markeev A and Zenkevich A 2015 Resistive switching and synaptic properties of fully atomic layer deposition grown TiN/HfO 2 /TiN devices *J Appl Phys* **117** 044901

[49] Kawai K, Kawahara A, Yasuhara R, Muraoka S, Wei Z, Azuma R, Tanabe K and Shimakawa K 2014 Highly-reliable TaOx reram technology using automatic forming circuit *2014 IEEE International Conference on IC Design & Technology* (IEEE) pp 1–4

[50] Rieck J L, Hensling F V E and Dittmann R 2021 Trade-off between variability and retention of memristive epitaxial SrTiO3devices *APL Mater* **9**

[51] Maikap S and Banerjee W 2020 In Quest of Nonfilamentary Switching: A Synergistic Approach of Dual Nanostructure Engineering to Improve the Variability and Reliability of Resistive Random-Access-Memory Devices *Adv Electron Mater* **6** 2000209

[52] Covi E, Brivio S, Serb A, Prodromakis T, Fanciulli M and Spiga S 2016 Analog memristive synapse in spiking networks implementing unsupervised learning *Front Neurosci* **10**

[53] Seo H K, Ryu J J, Lee S Y, Jeon K, Sohn H, Kim G H and Yang M K 2023 Analogue Artificial Synaptic Performance of Self-Rectifying Resistive Switching Device *Adv Electron Mater* **9**

[54] Park S, Sheri A, Kim J, Noh J, Jang J, Jeon M, Lee B, Lee B R, Lee B H and Hwang H 2013 Neuromorphic speech systems using advanced ReRAM-based synapse *2013 IEEE International Electron Devices Meeting* (IEEE) pp 25.6.1-25.6.4

[55] Kim T, Hu S, Kim J, Kwak J Y, Park J, Lee S, Kim I, Park J-K and Jeong Y 2021 Spiking Neural Network (SNN) With Memristor Synapses Having Non-linear Weight Update *Front Comput Neurosci* **15** 1–9

[56] Vatajelu E-I, Di Natale G and Anghel L 2019 Special Session: Reliability of Hardware-Implemented Spiking Neural Networks (SNN) *2019 IEEE 37th VLSI Test Symposium (VTS)* (IEEE) pp 1–8

[57] Diehl P U and Cook M 2015 Unsupervised learning of digit recognition using spike-timing-dependent plasticity *Front Comput Neurosci* **9** 1–9

[58] Querlioz D, Dollfus P, Bichler O and Gamrat C 2011 Learning with memristive devices: How should we model their behavior? *2011 IEEE/ACM International Symposium on Nanoscale Architectures* (IEEE) pp 150–6

[59] Lecun Y, Bottou L, Bengio Y and Haffner P 1998 Gradient-based learning applied to document recognition *Proceedings of the IEEE* **86** 2278–324

[60] Luo F, Zhong W-M, Tang X-G, Chen J-Y, Jiang Y-P and Liu Q-X 2023 Application of artificial synapse based on all-inorganic perovskite memristor in neuromorphic computing *Nano Materials Science*

[61] Siddik A, Haldar P K, Paul T, Das U, Barman A, Roy A and Sarkar P K 2021 Nonvolatile resistive switching and synaptic characteristics of lead-free all-inorganic perovskite-based flexible memristive devices for neuromorphic systems *Nanoscale* **13** 8864–74

[62] Moon K, Cha E, Park J, Gi S, Chu M, Baek K, Lee B, Oh S H and Hwang H 2016 Analog synapse device with 5-b MLC and improved data retention for neuromorphic system *IEEE Electron Device Letters* **37** 1067–70